ORNL/TM-2022/2629

Status Update on the Development of Transducers and Bonding Techniques for Enabling Acoustic Measurements of Damage in Microreactor Components

Anthony Birri
Daniel C. Sweeney
Holden C. Hyer
Christian M. Petrie

OAK RIDGE National Laboratory

ORNL IS MANAGED BY UT-BATTELLE LLC FOR THE US DEPARTMENT OF ENERGY

ORNL/TM-2022/2629

Nuclear Energy and Fuel Cycle Division

Status Update on the Development of Transducers and Bonding Techniques for Enabling Acoustic Measurements of Damage in Microreactor Components

Anthony Birri,
Daniel C. Sweeney,
Holden C. Hyer,
Christian M. Petrie

Milestone M4AT-22OR0804013
September 2022

Prepared by
OAK RIDGE NATIONAL LABORATORY
Oak Ridge, TN 37831
managed by
UT-Battelle LLC
for the
US DEPARTMENT OF ENERGY
under contract DE-AC05-00OR22725

CONTENTS

ACKNOWLEDGMENTS

This work is supported by the Microreactor Program of the US Department of Energys Office of Nuclear Energy. The authors acknowledge Adrian Schrell for providing a technical review.

ABBREVIATIONS

DAQ	data acquisition
FBG	Fiber Bragg grating
FPC	Fabry-Pérot cavity
LCI	low-coherence interferometry
MAGNET	Microreactor Agile Non-nuclear Experimental Testbed
MRP	Microreactor Program
MZI	Mach-Zehnder interferometer
OFDR	optical frequency domain reflectometry
OTDR	optical time domain reflectometry
SPHERE	Single Primary Heat Extraction and Removal Emulator
SWI	swept wavelength-based inferferometer

SUMMARY

This report provides an overview of potential sensors and sensor-bonding techniques to enable the online acoustic interrogation of microreactor components and enhance structural health monitoring capabilities. The report focuses primarily on optical fiber–based acoustic sensors and describes initial experimental progress toward the deployment of these sensors for microreactor applications. The general approach is to monitor the resonant frequencies of microreactor components and search for evidence of structural defects that could indicate imminent failure. If properly identified, then the components could be repaired during the next reactor outage to prevent costly unplanned shutdowns. The ability to monitor the structural health of components could also reduce the need for time-consuming visual inspections and reduce staffing to improve microreactor economic viability. Increased sensor density is also one of the first steps to moving toward eventual semiautonomous operation. The expected microreactor conditions in which acoustic sensors must survive are characterized, including temperatures, neutron fluences, thermomechanical strains, and vibrational frequencies. Optical fiber–based acoustic sensors are identified as an attractive candidate for acoustic monitoring because of their high accuracy, immunity to electromagnetic interference, and resiliency in high-temperature, high-radiation environments. Optical fiber–based intrinsic sensors, such as type-II fiber-Bragg gratings and Fabry-Pérot Cavities (FPCs), are particularly attractive for a microreactor environment because of their high temperature stability, and FPCs also enable higher frequency interrogation with a lower sensitivity to radiation-induced drift. This report describes multiple interrogation systems, but the best interrogation system for a given situation will depend on the specific microreactor application, including the desired acoustic vibrational amplitudes, modes, and resonant frequencies.

Initial experiments included fabricating three FPCs, tack-welding these FPCs to stainless-steel pipes or rods, and performing room-temperature acoustic sensing tests to capture the vibrational frequency content. Peaks were identified in the measured frequency spectra and compared with the theoretical fundamental frequencies obtained from Euler-Bernoulli beam theory. Two of the three FPCs measured vibrational frequencies that generally matched those obtained from theory. Future work will include similar testing on pipes or other microreactor components with intentional flaws to evaluate the ability to determine changes in resonant frequencies. Finally, these tests will be repeated at high temperatures, potentially with an applied thermomechanical stress, to include environmental conditions similar to those for a microreactor application.

1 INTRODUCTION

The US Department of Energy's Office of Nuclear Energy Microreactor Program (MRP) is focused on developing, maturing, and demonstrating technologies that will provide key support for future microreactor deployment. The MRP involves the joint efforts of multiple national laboratories and universities to conduct the fundamental and applied research required to meet the programmatic goals. Microreactors present the opportunity to tap into unconventional nuclear markets, such as remote communities, mining sites, military bases, and disaster relief programs [1]. The primary differences between microreactors and light-water reactors or small modular reactors are that microreactors (1) may be fully assembled in a factory and shipped to a desired location, (2) can be transported with multimodule transportation, and (3) may be controlled remotely and semiautonomously [2]. The MRP is primarily focused on developing heat pipe–cooled reactors [3, 4], gas-cooled reactors [5], and liquid metal–cooled reactors. The MRP is

developing two nonnuclear systems to serve as experimental test beds to evaluate the thermal-hydraulic and thermomechanical behavior of microreactor components. The Single Primary Heat Extraction and Removal Emulator (SPHERE) [6] facility is being used to evaluate heat rejection from single heat pipes, and the MAGNET (Microreactor AGile Non-nuclear Experimental Testbed) facility [7] is being used to evaluate larger heat exchangers and the integral thermal hydraulic performance of larger microreactor components, such as an array of heat pipes with electrical heaters to simulate nuclear heating.

One enabling technology for microreactors is the ability to perform in situ structural health monitoring to identify the need for preventative maintenance, prevent unplanned reactor shutdowns, and reduce operation and maintenance costs via reduced staffing that would otherwise be needed to perform time-consuming visual examinations. Because of the small size of these microreactors, large temperature gradients are expected throughout the reactor core, which could induce differential thermal strains in the reactor core components. The small core size also lends itself to higher neutron leakage and larger neutron flux gradients, which could result in spatial variations in radiation-induced swelling or other dimensional changes that would also cause concern for the structural health of in-core components. Ideally, these strains could be monitored in real time to ensure the structural health of the core components. To this end, the MRP is pursuing sensor technologies that can detect structural defects and characterize, for example, the number, size, location, and orientation of any cracks or other defects that may form. These health-monitoring technologies could have applications during nonnuclear experimental testing, irradiation testing in materials test reactors, intermittent measurements during outages, or in situ measurements during microreactor operations. In the latter case, online health-monitoring capabilities could be integrated into automated or semiautonomous control systems that combine a wealth of information from sensors and digital twins to inform the control system's response [8]. The ability to reduce operation and maintenance costs through enhanced monitoring technologies and reduced staffing is also crucial for making these low-power reactor designs economically viable.

One common method for detecting the formation of cracks and other structural defects in structural components is to monitor the structure's vibrational modes or resonant frequencies. With appropriate spatial and frequency resolution, acoustic- or vibration-based damage detection offers the advantage of determining both the location and size of damage [9]. Identifying the fundamental frequencies, or *eigenfrequencies*, and determining how shifts in these frequencies correspond to damage scenarios is a popular acoustic-based method [10]. Other methods involving changes to modal properties exist, including methods based on changes in mode shape and mode shape curvature [11]. Unlike some of these more traditional methods, recent work has investigated the use of machine learning or deep learning for structural health monitoring [12].

Regardless of the method chosen for structural health monitoring in microreactors, sensors used to obtain frequency-dependent strain data must (1) provide a sufficiently wide bandwidth to capture the fundamental frequency information associated with the microreactor component geometry, (2) be embedded or otherwise integrated into the component's structure without being too intrusive, and (3) provide accurate data for an extended duration in a high-temperature, high-neutron/gamma radiation environment. Additionally, having acoustic sensors that can be spatially distributed throughout the component for improved damage localization and magnitude determination would be ideal. Finally, it would also be ideal if these sensors could resolve particularly small frequency changes that may correspond to small defects, such as microcracks. This report investigates potential acoustic sensors for microreactor vibration measurements with a focus on optical fiber–based sensors. Initial experimental studies and plans using one example of an optical fiber–based sensor are also reported.

2 INVESTIGATION OF CANDIDATE VIBRATION SENSORS

2.1 Microreactor Sensing Requirements

Generally, microreactor environments are extremely harsh for sensors, especially acoustic sensors that must be mechanically coupled to structural components. Acoustic sensors for microreactors must survive high temperatures, high neutron flux/fluences, and large thermomechanical strains, all while providing the required spatial, temporal, and strain resolution. Although the specific requirements may vary from one microreactor design to another and publicly available information for specific microreactor concepts is limited, this report aims to identify and quantify realistic requirements for acoustic sensors in microreactor applications.

Numerous thermal modeling efforts regarding microreactor operating temperatures have been conducted to calculate representative temperatures for microreactor core components. These thermal modeling efforts have been largely focused on heat pipe–cooled microreactor designs. Mathews et al. modeled a Los Alamos National Laboratory-developed heat pipe–cooled microreactor operating at 2 MWth whose maximum monolith and heat pipe surface temperatures were 853 and 815°C, respectively [3]. Fei et al. modeled a molten metal–fueled, heat pipe–cooled microreactor using a full-core analysis that resulted in a maximum heat pipe wall temperatures slightly exceeding 855°C for some transient conditions [13]. Sterbentz et al. analyzed three different 5 MWth heat pipe–cooled designs and reported maximum heat-pipe wall temperatures of 712.5, 677, and 712.5°C for each of these designs [14, 15]. Therefore, for heat pipe–based microreactors that integrate heat pipes within monolithic metal structures, acoustic sensors would be required to survive temperatures up to 800–900°C to provide data regarding the structural health of the monolithic core block.

Publicly available data for the expected neutron flux or fluence to which microreactor components would be exposed are more limited. Sterbentz et al. reports a fast flux at the core midplane of 5.5×10^{13} n/cm^2/s for a heat pipe–cooled microreactor [14]. For constant operation times of 1, 5, and 20 years, this would correspond to fast neutron fluences of 1.73×10^{21}, 8.67×10^{21}, and 3.47×10^{22} n/cm^2, respectively. Depending on the desired component lifetime and its location in the core, acoustic sensors could be required to survive fast neutron fluences as high as 10^{22} n/cm^2, assuming that periodic sensor replacement is infeasible because of the required bonding between the sensors and the monolith or heat pipe walls. The radiological hazards associated with sensor replacement would likely require remote welding/bonding operations that would be particularly challenging, especially when bonding fragile sensors. These time-consuming operations would likely mitigate any cost benefits associated with the enhanced health-monitoring capabilities gained by using the acoustic sensors.

Like neutron flux, little information is available regarding thermally induced strain. Petrie et al. determined stresses and strains at a location where an embedded sensor would exist within a heat pipe–cooled monolithic block with cartridge heaters to simulate microreactor heating in Idaho National Laboratory's SPHERE facility [16]. With a relatively small test article and a relatively low thermal power of ~1,900 W (250.2 kW/m^2 heat flux to the heat pipe), the thermal strain on the outer surface of the test article ranged from 40 μm/m with BN paste filling the gap between the cartridge heater and test article to as high as 74 μm/m with a He-filled gap. The maximum y-axis and z-axis stresses occurred on the inner surface of the test article with the lowest temperatures. These stresses were 198 and 224 MPa, respectively, when using a

He-filled gap. Significantly higher stresses and strains may be expected in an actual microreactor operating with thermal powers on the order of approximately megawatts thermal and potentially having much larger thermal temperature gradients.

Bonded acoustic sensors would also be subject to differential thermal stresses due to the difference in the thermal expansion coefficient between the optical fiber and the test article. These stresses will depend on the test article thermal expansion coefficient, test article temperature when the sensor-test article bond occurs, and length of the bonded region. For example, these differential stresses can be reduced by using a smaller bonded length for an Fabry-Pérot Cavity (FPC) vs. bonding a long length of fiber that contains multiple fiber Bragg gratings (FBGs) to provide spatially distributed measurements. Without taking advantage of shorter embedded lengths, embedded fiber-optic sensors can survive differential stresses up to 500°C in Al [17] and ~450°C in stainless steel [18, 19] before the fiber breaks or de-bonds from the test article. Future work under this activity will focus on identifying appropriate sensors and bonding techniques, including the length of the embedded region, to survive the expected operating temperatures for various microreactor applications.

Finally, it is important to consider the range of frequencies that may contain pertinent information for structural health monitoring in a nuclear microreactor. Low fundamental modes on the order of hertz to tens of hertz associated with the vibration of the entire structure of a large power reactor are expected, based on the theoretical works in Luz et al. [20] and the computational methods performed in Verma et al. [21]. Higher resonant frequencies are expected for reactor system components, such as pipes or individual fuel assemblies, and these frequencies could be in the range of hundreds of hertz to tens of kilohertz [22, 23]. Smith and Agarwal observed significant contributions to the frequency spectrum in the range of 1 to 10 kHz from acoustic receivers mounted to the pressure vessel wall of the Advanced Test Reactor [24]. Finally, even higher frequencies could be monitored in the range of 50 to 300 kHz, which is associated with acoustic emission frequencies of various reactor components [25]. Considering that vibrational frequencies could vary over several orders of magnitude, acoustic sensors should be chosen based on specific application-based requirements. For the purposes of this work, interrogation techniques that can measure resonant frequencies on the order of hundreds of kilohertz were evaluated to extract as much vibrational information as possible for structural health-monitoring purposes.

2.2 Candidate Sensors

Many types of vibration sensors exist, but few are capable of in situ deployment in the aforementioned microreactor environment. Noncontact sensors are not being considered in this report because of the difficulties in optically accessing the component and aligning laser beams, especially if access requires penetrating a pressure boundary. Opaque coolants such as liquid metals and some liquid salts would also be incompatible with noncontact optical measurements of in-core components. Noncontact methods could be considered for some ex-core components.

The three major types of contact sensors for acoustic monitoring include resistive strain gauges, piezoelectric accelerometers, and fiber-optic sensors. Resistive strain gauges can provide reliable measurements of static and dynamic (on the order of tens of hertz) strain during irradiation testing to moderate fast neutron fluences up to $\sim 10^{20}$ n/cm^2 in air or under pressurized water conditions (300°C or less) [26, 27]. Resistive strain gauges are also relatively large, are generally limited to temperatures below 400–500°C, and have lower sensitivity, which makes them better suited for monitoring large static strains

than smaller dynamic strains.

Piezoelectric sensors such as $Bi_4Ti_3O_12$, $LiNbO_3$, $BaTiO_3$, $Pb[Zr_xTi_{1-x}]O_3$ ($0 \leq x \leq 1$), and ZnO generally have shown significant degradation during neutron irradiation [28, 29]. Aluminum nitride piezoelectric sensors have survived fast neutron fluences up to 6×10^{20} n/cm^2, although some pulse echoes could no longer be observed and other amplitudes decreased by ~57% [28]. Measurements of the AlN sensor could only be resolved after reactor shutdown, not during reactor operation. Magnetostrictive transducers were found to be more tolerant of fast neutron irradiation up to 6×10^{20} n/cm^2 and could be considered for measuring vibrational frequencies on the order of hundreds of kilohertz or lower [28]. Resistive and piezoelectric sensors also suffer from electromagnetic interference.

Bulk amorphous fused silica, which is the primary choice for optical fiber material, has reasonable optical transmission in the near infrared wavelength region that is commonly used for sensing, even at fast neutron fluences of 2.4×10^{21} n/cm^2 [30]. Work is currently being conducted to test optical fibers in higher fluences. For example, ongoing tests in the High Flux Isotope Reactor have now achieved a maximum fast neutron fluence of ~10^{21} n/cm^2 and plan to reach a maximum fast neutron fluence as high as ~3×10^{21} n/cm^2 [31]. Those tests show minimal signal attenuation in optical fibers with pure silica core and F-doped silica cladding. Other tests have shown a very manageable signal attenuation of ~6 dB in optical fiber–based sensors with an irradiated length of ~40 cm that was exposed to a fast neutron fluence on the order of ~3×10^{20} n/cm^2.

Aside from the knowledge of survivability at higher fluences, optical fibers also offer several other advantages over electrical-based sensors, such as being extremely small (~100 μm diameter), having immunity to electromagnetic interference, and having distributed sensing—or at least quasidistributed sensing capabilities, depending on the application. The extremely small size of optical fibers is especially useful in microreactor applications because the sensor does not have significant volume and does not require significant geometric changes to the component to accommodate the sensor (e.g., thinning of structural walls). Because of these advantages, the remainder of this document focuses on optical fiber–based acoustic sensors.

2.3 Fiber-Optic Sensors

Various intrinsic or extrinsic optical fiber–based sensors could be considered for acoustic sensing in microreactor applications. These sensors must be robust under the temperatures and fluences described in Section 2.1. Unmodified optical fibers can be used to perform distributed strain sensing using optical frequency domain reflectometry (OFDR) or optical time domain reflectometry (OTDR) by analyzing light that is reflected along the length of the fiber from Rayleigh or Brilloiun scattering [32]. OFDR-based measurements are limited in the maximum vibrational frequency that can be resolved due to the time required to scan a tunable laser. For example, the highest scan rate for state-of-the-art OFDR-based sensing systems provided by Luna Innovations Inc. is 250 Hz.

Unmodified optical fibers are commonly interrogated using OTDR to perform distributed acoustic sensing [33]. The challenge with OTDR-based techniques is that short laser pulse (< 10 ns) widths are required to achieve even meter spatial resolution—too large for microreactor components—at frequencies on the order of kilohertz. Higher frequency vibrations can be resolved at the cost of shorter sensing lengths. Short pulse widths also translate to weaker signals that limit the total sensing length due to intrinsic fiber attenuation, reduce the strain sensitivity, and are more susceptible to radiation-induced attenuation of the light signal.

FBGs can be inscribed into optical fibers to enhance the reflectivity over a very narrow wavelength range. A depiction of an FBG is shown in Figure 1 (b). An FBG is a modulation of the refractive index along the core of an optical fiber, which is typically achieved by inscription with a high-powered laser through a phase mask or a point-by-point technique. When light is transmitted down the fiber and impinges upon the grating, the reflected spectrum of light contains one peak, often with side lobes, as a consequence of constructive interference of the various light contributions from each modulation along the grating at slightly different phases. Type-II FBGs are inscribed with a femtosecond-laser and are inscribed above the damage threshold of glass, which results in an FBG with survivability up to 1,000°C [34]. Zaghloul et al. demonstrates that type-II FBGs in random air-line fibers showed a less than 5 dB reduction in FBG peak strength after $> 1 \times 10^{20}$ n/cm^2 [35]. The survivability of type-II FBGs at higher fluences is unclear but is being studied, according to Petrie et al. [31]. FBGs could be suitable candidates for microreactor health monitoring, depending on the method of interrogation, as discussed in Section 3.2. However, there may be challenges in identifying a suitable technique for bonding long lengths of fiber containing multiple FBGs to microreactor components and ensuring that the fiber survives at high temperatures due to the large difference in thermal expansion coefficients of most metals and the optical fibers. Additional work is needed to evaluate temperature limitations for various bonding techniques.

FPCs are often used for single-point static or dynamic strain monitoring. These cavities comprise an air gap between either two optical fibers (i.e., an intrinsic FPC) or an optical fiber and an external reflective surface (i.e., an extrinsic FPC). A depiction of an FPC is shown in Figure 1(a). Similar to distributed measurements, FPCs can be interrogated using time domain or frequency domain interferometry. Light is partially reflected at the first fiber-air interface and transmitted to the second interface between air and a second fiber or other material where an additional reflection occurs. The two reflected light beams combine to form an interference pattern in the time or frequency domain. In the frequency domain, this manifests as a series of peaks. Because FPCs can include highly reflective surfaces and can be interrogated using intense laser-based light sources, these sensors can withstand significant radiation-induced signal attenuation. Depending on the interrogation technique, as discussed in Section 3.2, FPCs are capable of measuring strains on the order of micrometers per meter or lower at frequencies on the order of megahertz. One disadvantage of using FPCs is that they can typically only provide one spatial measurement, although efforts have been made to demonstrate cascaded FPCs within one optical fiber [36]. Alternatively, the Spallation Neutron Source at Oak Ridge National Laboratory currently deploys >20 FPC-based vibration sensors using a multichannel data acquisition (DAQ) system [37]. Therefore, there is precedent in deploying an array of FPC-based vibration sensors in a very high radiation environment. FPC sensors can also provide a stable response at temperatures up to 1,100°C [38].

For these reasons, the authors chose to focus initially on experimental work under this program, primarily on the development of FPC-based sensors for in situ acoustic monitoring of microreactor components. FBGs could be bonded to microreactor components over much shorter lengths than longer lengths of fibers with multiple inscribed FBGs. This could enable higher temperature operation by reducing the thermal strain on the fiber and the FPC. However, type-II FBGs may be a viable option for some applications that require fine spatial resolution at frequencies on the order of kilohertz or lower. Section 3.2 discusses techniques for interrogating FPCs, some of which could also be applied to FBGs.

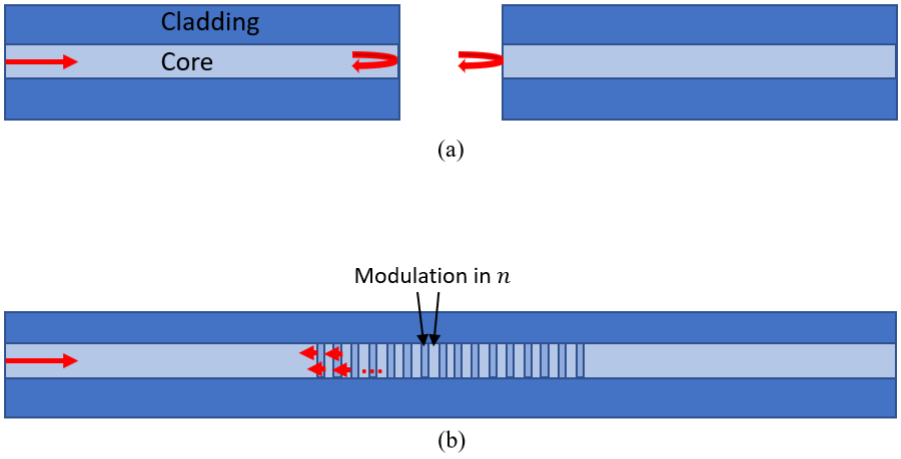

Figure 1. (a) Depiction of an FPC; (b) depiction of an FBG.

3 METHODS

3.1 Theoretical Calculations

Theoretical calculations are performed to provide a reference against which the experimentally measured vibrational frequencies can be compared. For the experimental work considered herein, the test articles used for vibrational measurements were either metal pipes or rods. Their free vibration is described by Bernoulli-Euler beam theory. The test articles are freely hanging and can be considered beams in a free-free configuration.

The natural angular frequencies that satisfy the governing free vibration equation for a beam are defined as

$$\omega_n = {\beta_n}^2 \sqrt{EI/\rho_L}, \tag{1}$$

where ω_n is the angular frequency of the nth mode, β_n is the wavenumber of the nth mode, E is the Young's modulus, I is the area moment of inertia, and ρ_L is the linear density.

The eigenvalues associated with the solution are given as $\beta_n L$, where L is the length of the beam. For the boundary conditions associated with a free-free configuration, the eigenvalues that satisfy the governing differential equation are defined as

$$\cosh(\beta_n L)\cos(\beta_n L) - 1 = 0. \tag{2}$$

Disregarding $\beta_n L = 0$, the first four roots of Eq. (2) result in the following fundamental frequencies (f_1 through f_4) for a free-free beam after inserting these roots into Eq. (1) and converting to ordinary

frequency:

$$f_1 = \frac{22.373}{2\pi L^2}\sqrt{\frac{EI}{\rho_L}}, \tag{3}$$

$$f_2 = 2.757 f_1, \tag{4}$$

$$f_3 = 5.404 f_1, \tag{5}$$

$$f_4 = 8.402 f_1. \tag{6}$$

Silva, Nascimento, and dos Santos [39] provide a complete derivation that leads to these fundamental frequencies. In Eq. (3), I can be determined by:

$$I = \frac{\pi}{64}(d_o^4 - d_i^4), \tag{7}$$

where d_o and d_i are the outer and inner diameter of the test article, respectively ($d_i = 0$ for a rod). ρ_L can be determined by:

$$\rho_L = \frac{\pi}{4}(d_o^2 - d_i^2)\rho, \tag{8}$$

where ρ is the volumetric density of the test article.

3.2 Interrogation Systems for Optically Based Sensors

3.2.1 Spectrometery System

FPCs can be interrogated using several inexpensive components—such as an optical circulator, broadband light source, and line-scan camera or spectrometer—while achieving suitable performance to monitor vibrations in a test article, as shown in Figure 2(a). In such a configuration, the light source, such as a superluminescent diode, injects light into an FPC through the optical circulator. The light reflected from the two interfaces within the FPC is coupled back into the optical fiber and produces a spectral interference pattern at the spectrometer after traveling back through the circulator. The interference pattern is read out through a DAQ interface. The optical intensity of the spectrum (I_R) returned to the spectrometer is given by

$$I_R(\lambda) = I_0\left[\frac{(\sqrt{R_1} - \sqrt{R_2})^2 + 4\sqrt{R_1 R_2}\sin^2(\phi/2)}{(1 - \sqrt{R_1 R_2})^2 + 4\sqrt{R_1 R_2}\sin^2(\phi/2)}\right], \tag{9}$$

where R_1 and R_2 are the reflectivites of the fiber-cavity and cavity-fiber interfaces, respectively; I_0 is the intensity of the incident light; and λ is the photon wavelength.

The optical phase difference between the two reflections, ϕ, is given by

$$\phi = \frac{4\pi n_g l}{\lambda}, \tag{10}$$

where n_g is the group index of the fiber, and l is the length of the FPC cavity. The component strain can be determined from the change in the FPC length, $\Delta l(t) = l(t) - l_0$, relative to the initial FPC length, l_0, after dividing by l_0.

Using a phase tracking approach, the strain, $\varepsilon(t)$, as a function of time, t, can be determined by tracking the relative change in any peaks in the interference pattern:

$$\varepsilon = \frac{\Delta l(t)}{l_0} = \frac{\Delta \lambda(t)}{\lambda_0}, \tag{11}$$

where $\lambda_0 = \lambda(t_0)$. Recording $\lambda(t)$ over the time interval $[t, t + T]$ produces a series of strain measurements that can be used to calculate the power spectral density $S_T(t)$ of the strain over interval T to characterize the vibrational modes of the test article. Namely,

$$S_T(t) = \frac{1}{T}\mathcal{F}\Big\{\varepsilon^*(-t) \otimes \varepsilon(t)\Big\}, \tag{12}$$

where $\mathcal{F}\{\cdot\}$ indicates the Fourier transform, and $*$ indicates the complex conjugate.

Using a broadband source and spectrometer to monitor acoustic strains offers several benefits, including a relatively simple optical setup and the potential to interrogate FPCs or an array of FBGs through wavelength division multiplexing. Sampling rates on the order of ~10 kHz are possible, depending on the specific spectrometer used [40]. However, this requires a strong light source and minimal signal attenuation to allow for short integration times. Moreover, the wavelength resolution of most spectrometers is typically far less than the wavelength accuracy of tunable lasers, which results in much lower strain resolution when using broadband light and a spectrometer vs. a tunable laser-based interrogation system. Signal processing using curve fitting methods to identify peak maxima in an optical spectrum can improve measurement resolution but still requires a sufficiently large number of samples and measurement stability to be useful [41]. For these reasons, the combination of a broadband source and spectrometer could be suitable for some microreactor applications, depending on the specific strain, spatial, and temporal requirements and the expected radiation-induced attenuation of the light signal.

3.2.2 Swept Wavelength-Based System

One alternative to using a broadband light source for interrogating an FPC is to use a tunable laser-based interferometry system, as shown in Figure 2(b). One such system is the Hyperion series of instruments (Luna Innovations Inc., Blacksburg, Virginia). These instruments rely on a tunable laser source that is swept over a wavelength range on the order of 10 to 100 nm. The transmitted light is compared with a known reference wavelength to produce an interference pattern, which is recorded with a photodetector (PD1) to track the instantaneous wavelength of the tunable laser source. Light that is reflected from the FPC is returned to a second photodetector (PD2) that measures the reflected intensities as the wavelength of the tunable laser is varied. This produces a spectral interference pattern that is the same as that in Eq. (9). The strain calculation and the subsequent PSD operation proceed in a manner similar to the spectrometer-based setup.

Swept wavelength-based interferometrs (SWIs) benefit from higher wavelength resolutions—and associated strain resolution—of 0.1 pm and light intensities compared with what can be achieved using a broadband light source and spectrometer. However, this comes at the cost of a slower DAQ rate on the

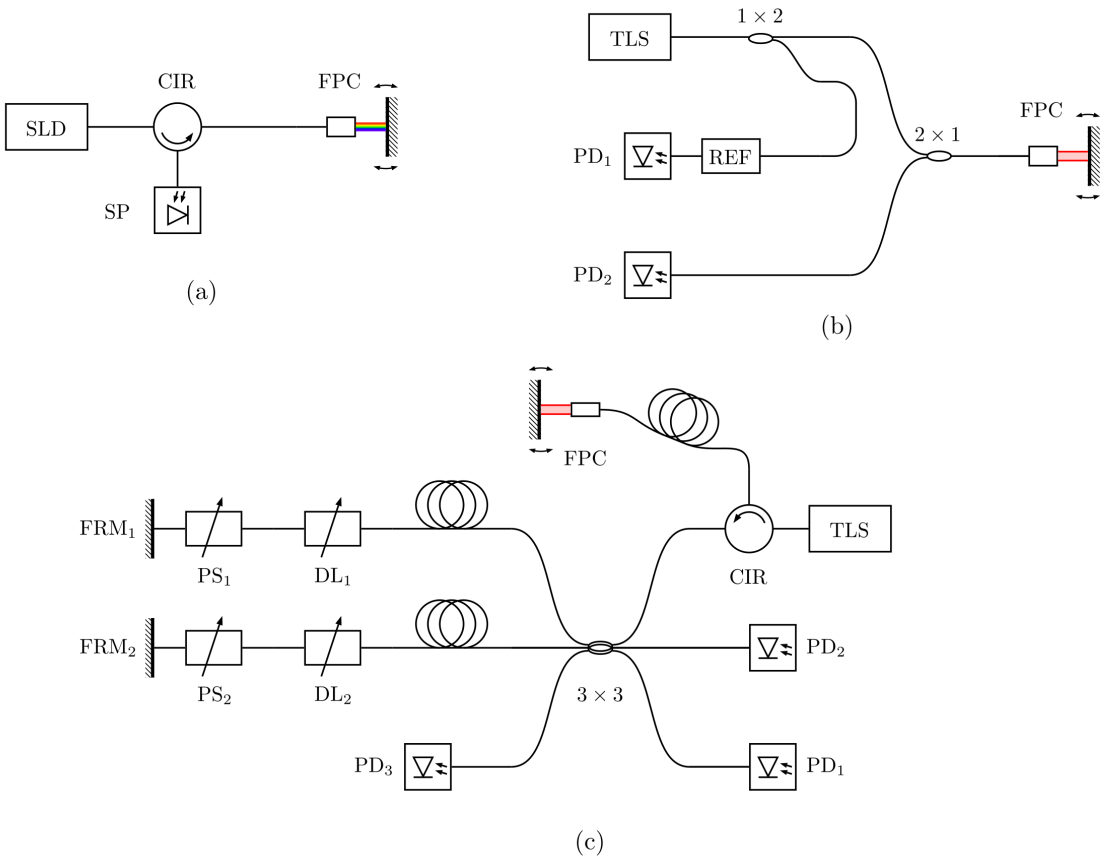

Figure 2. Optical interrogator toplogies considered for vibration measurements, including (a) a two-photodetector, swept wavelength spectral interrogator, (b) a spectrometer-based FPC interrogator, and (c) a low-coherence interferometry (LCI) system.

order of kilohertz. Therefore, SWI-based measurement systems are a suitable choice for interrogating FPCs or FBGs for applications that require high signal intensities—or large radiation-induced light attenuation—to monitor components with resonant frequencies in the hertz to kilohertz range. Advanced signal processing and demodulation strategies were developed to extend the accuracy of phase-tracking techniques with SWI measurements to a wider range of displacements [42, 43].

3.2.3 Low-Coherence Interferometry System

An all-fiber LCI system can be used to interrogate FPC sensors with nanometer displacement precision at extremely high sampling rates. For example, previous works have demonstrated DAQ at frequencies of > 100 kHz [44, 45], and higher frequencies could be resolved using the same optical interferometer with a faster DAQ system. The LCI system used in the present work comprised a broadband, low-coherence light source coupled into an FPC through an optical circulator before returning through the circulator and entering a Mach-Zehnder interferometer (MZI). The MZI comprises a local interferometer in which the two arms of the MZI are offset by a constant phase $z_0 \in [-\pi, \pi]$ and are collocated in a benign environment to mitigate unsymmetrical polarization changes between each leg. The light entering each leg passes through a delay line and a phase shifter before being reflected by a Faraday mirror and recombining in a 3×3 coupler. After recombination, the interferring light enters two photodetectors, and the change in FPC length can be demodulated from the interference patterns measured by the two photodetectors.

As described previously [44, 45], the time-dependent FPC length in the sensor can be determined based on the normalized ratio $R(t) = A_1(t)/A_2(t)$ of the measured signals from PD1 (A_1) and PD2 (A_2). This assumes that the light source has a sufficiently large coherence length $l_c^2 \gg \lambda|x(t)|$, where l_c is the coherence length of the light source, and $x(t)$ is the optical path length difference between the local and sensing interferometers. In practice, the delay lines in the local interferometer are adjusted until the path length differences in the local interferometer match the FPC length in the sensor to within l_c. When the assumption regarding l_c is satisfied, the length of the FPC can be demodulated from one of two estimates of the change in cavity length, $\Delta l_1(t) = l(t) - l_0$ and $\Delta l_2(t) = l(t) - l_0$, relative to an initial length $l_0 = l(t_0)$:

$$\Delta l_1(t) = \frac{\lambda}{4\pi}\left[\arctan\left(\frac{1}{\tan(z_0)} - \frac{1}{R(t)\sin(z_0)}\right)\right], \tag{13}$$

$$\Delta l_2(t) = \frac{\lambda}{4\pi}\left[\arctan\left(\frac{R(t)}{\sin(z_0)} - \frac{1}{R(t)\tan(z_0)}\right) - z_0\right]. \tag{14}$$

These two estimates produce similar values for $\Delta l(t)$, except near $R = \pm 1$ or when the normalized signals from PD1 and PD2 are equal in magnitude. The change in FPC length can be demodulated without error if the sampling frequency is high enough to avoid phase ambiguity. In order to produce valid measurements, the sampling frequency f_s must satisfy

$$f_s \geq \frac{32\pi f_0 \Delta x}{\lambda(1 - |1 - 2z_0/\pi|)}, \tag{15}$$

where f_0 is the frequency of the deflection Δx [45]. The change in FPC length over time through the continuous summation of discrete samples at time t_i is

$$\Delta l(t_i) = \Delta l(t_{i-1}) + \begin{cases} \Delta l_1(t_i) - \Delta l_1(t_{i-1}), \text{ if } |4\pi\Delta l_2(t_i) + z_0\lambda| > |4\pi\Delta l_1(t_i)|, \\ \Delta l_2(t_i) - \Delta l_2(t_{i-1}), \text{ otherwise} \end{cases} . \tag{16}$$

Table 1. Comparison of optical interrogation systems.

Method	Acquisition rate (kHz)	Signal-to-noise ratio	Displacement resolution (nm)	Reference
Spectrometry	~10	Low	<5	
SWI	~1	High	~2	[42, 43]
LCI	>100	Low	~2	[45, 44]

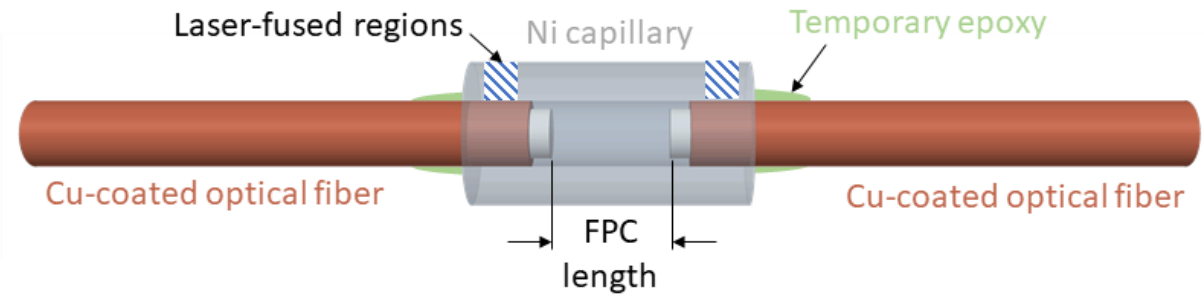

Figure 3. Schematic of an FPC sensor, including the temporary epoxy used to hold the fibers inside the capillary tube before fusing the capillary tube to the fibers with a laser.

The specifics of this and several other related phase demodulation strategies have been developed and are implementable in hardware to achieve sampling rates >1 MHz [45, 44].

4 EXPERIMENTAL PLANS AND INITIAL RESULTS

4.1 Fabry-Pérot Cavity Fabrication

Extrinsic FPCs were fabricated by locally melting a commercially available Ni capillary tube at both ends that contains metal-coated optical fibers inserted from both ends (Figure 3). This minimizes the mechanical strain to which the fiber is exposed at high temperatures because the metal test articles expand more than the fused silica optical fibers. Using a Ni capillary tube also makes it easier to join the FPC to the test article via standard welding/joining techniques. The selection of commercially available metal-coated optical fibers is limited to Al, Au, or Cu coatings. Nickel coatings are commercially available in short lengths on the order of centimeters, which is long enough to fabricate an FPC but not long enough to route the Ni-coated portion of the fibers outside a high-temperature experiment. Conventional polymer-coated fibers can survive temperatures up to ~1,000°C, but they are very fragile after the polymer coatings burn off. Copper-coated fibers were chosen because of the high melting point of Cu, its flexibility for ease in handling, and its compatibility with the Ni capillary tubing. The Cu-coated fibers (IVG Fiber) had a Ge-doped 9 μm fused silica core, a 125 μm pure fused silica cladding, and a coating diameter of 165 μm.

An FPC was formed by inserting two sections of the the Cu-coated fiber into a Ni capillary (Vici Valco) with a 178 μm inner diameter and a 355 μm outer diameter. The ends of the two fibers were first cleaved to produce a flat surface and then inserted into a ~25 mm section of the Ni capillary. One fiber was temporarily epoxied at the point at which it enters the capillary tubing so that it terminated near the tubing center. The second fiber was manually manipulated while measuring the FPC length using a tunable

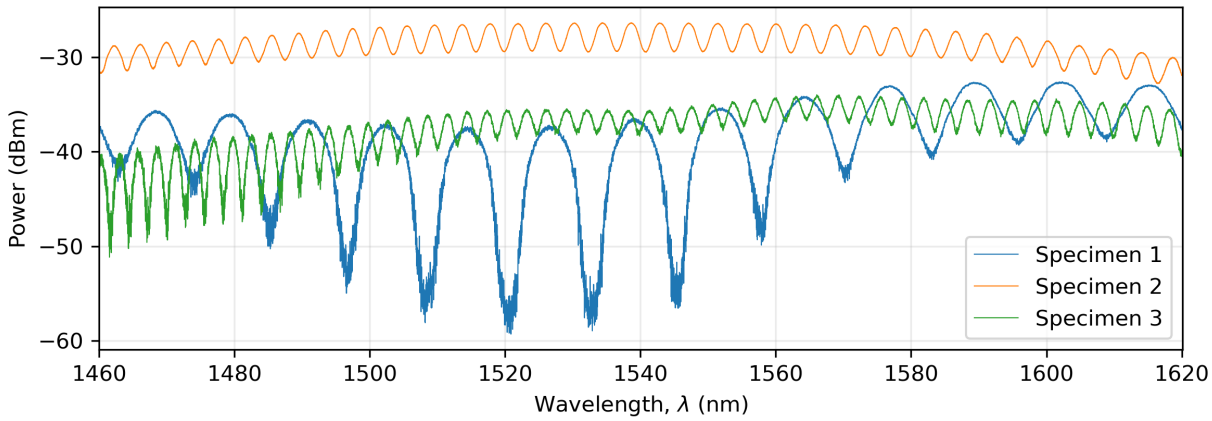

Figure 4. Optical spectra of the FPCs attached to specimens 1, 2, and 3 acquired using a Hyperion si155 instrument.

laser-based interrogation system, as described in Section 3.2. Once the proper cavity length was achieved (generally 100–400 μm), the second optical fiber was epoxied at the point at which it enters the capillary tubing. Next, a Renishaw AM400 laser powder bed fusion system was employed to locally fuse the Ni capillary tube to each fiber. The sensors to be fused were laid flat on a stainless-steel hearth in the focus of the scanning laser. A 5 mm section, distanced ~5 mm from the ends of the two fibers, was scanned using a laser power of 200 W and raster speed of ~600 mm/s. The laser scanned perpendicular to the axial direction of the sensor with a distance between consecutive scans set to 400 μm. The resulting optical interference spectra obtained from the FPCs used with each specimen are shown in Figure 4.

4.2 Demonstration of Optical Interrogation System

Initial experiments are being performed to demonstrate the capability to detect the fundamental vibrational frequencies in metal pipe or rod specimens. These experiments will be repeated after introducing a defect or changing boundary conditions to determine whether the interrogation system can detect any changes in resonant frequencies. If successful, similar experiments will be performed at relevant microreactor temperatures to determine whether the FPCs are well suited for high-temperature applications or if other sensors should be investigated. Table 2 summarizes the three specimens that are being tested, which include pipes with varying dimensions and a solid rod. All specimens were fabricated of 304 stainless steel.

A diagram of the experimental setup for eventual high-temperature testing is shown in Figure 5. The specimen will be suspended in the furnace via a string or wire, which will be fed through 1.6 mm (1/16 in.) diameter holes located near the top of each specimen. FPCs will be bonded to the specimens by placing stainless-steel strips over the FPCs and tack-welding the strips to the specimen on either side of the FPC. This configuration will enable the FPC to be tested at high temperatures with a reference piezoelectric accelerometer located outside the high-temperature region for comparison. The FPC may be monitored with the LCI system, as indicated by Figure 5, or the Hyperion (SWI) system. The accelerometer will be monitored with an off-the-shelf DAQ system from National Instruments.

Table 2. Experimental test matrix for measuring vibrational frequencies with high-temperature FPCs.

Specimen	Outer diameter (cm)	Inner diameter (cm)	f_1 (Hz)	f_2 (Hz)	f_3 (Hz)	f_4 (Hz)
1	1.27	1.17	90	249	488	759
2	1.905	1.73	135	371	727	1131
3	1.27	N/A	66	183	359	558

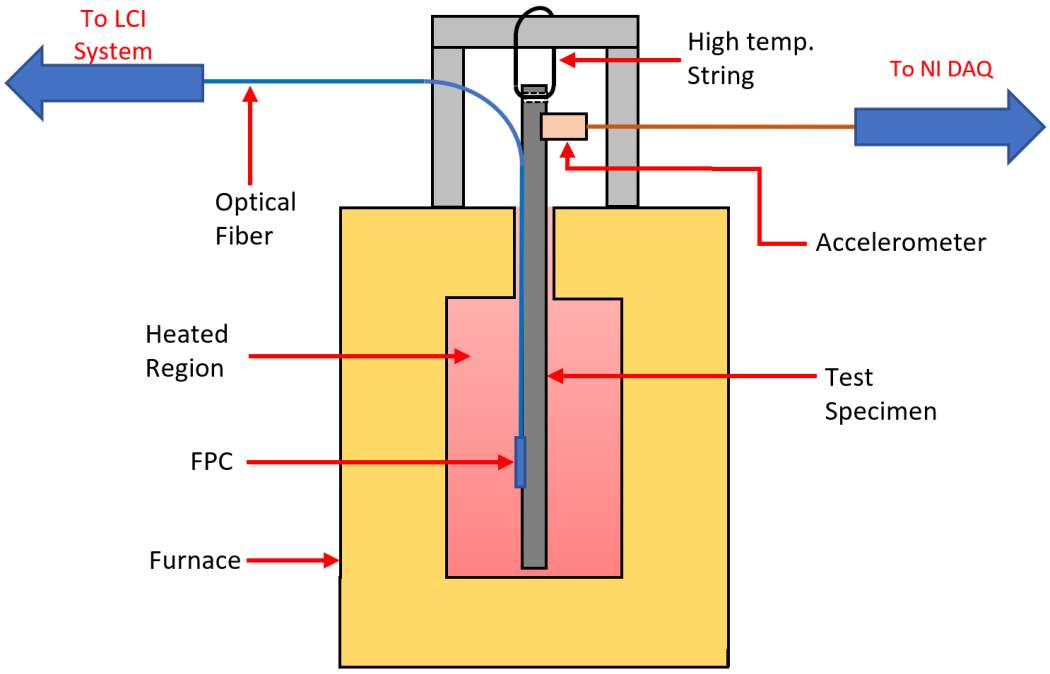

Figure 5. Planned experimental setup to measure the vibrational frequencies of various specimens at high temperatures using an FPC and at low temperatures using an accelerometer.

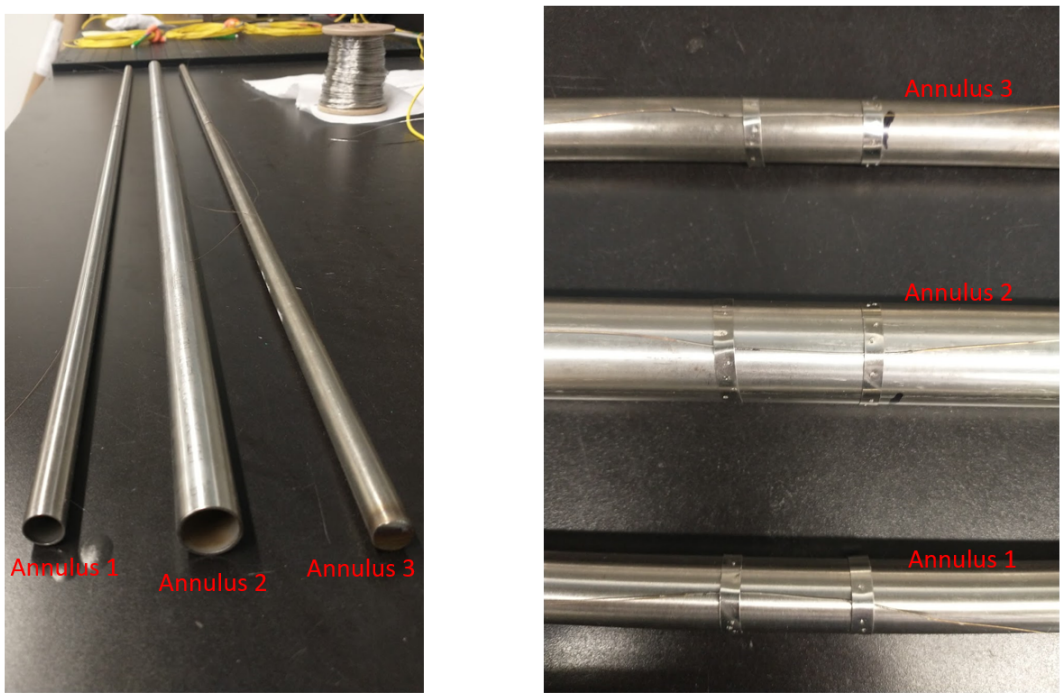

Figure 6. (a) The three specimens described in Table 2; (b) Close-up view of the FPCs bonded to each specimen by tack welds.

4.3 Initial Experimental Results

Figure 6 shows photographs of FPCs that have been bonded to each of the three specimens described in Table 2. The expected fundamental frequencies for each specimen were calculated per Eqs. (3)–(8) and are summarized in Table 2.

Initial measurements of each specimen were made at room temperature by suspending the specimen with metal wire. The FPCs were interrogated using the LCI system to obtain dynamic deflections with a sampling rate of 100 kHz. Impulse responses were observed by striking the samples with a metal rod. Figures 7, 8, and 9 show the vibrational amplitudes as a function of time and frequency for specimens 1, 2, and 3, respectively. The frequency content was obtained by performing a fast Fourier transform of the time-dependent displacement data over 0.5 s intervals. The Fourier transforms were performed in Python version 3.9.7 using the `numpy.fft.fft` function in NumPy version 1.21.2. Theoretical frequencies from Table 2 are shown as black dashed lines in the plots. These data are also visualized in 2D plots for each specimen at the 0.5 s time interval after striking the specimens in Figure 10. The signal amplitude is normalized to each respective maximum amplitude in Figure 10.

The measured vibrational frequencies generally matched the theoretical values, and better agreement was observed in specimens 2 and 3. The lowest resonant frequency measured from the FPC that was bonded to specimen 1 matched theoretical values. Some evidence suggests experimental peaks near the second and

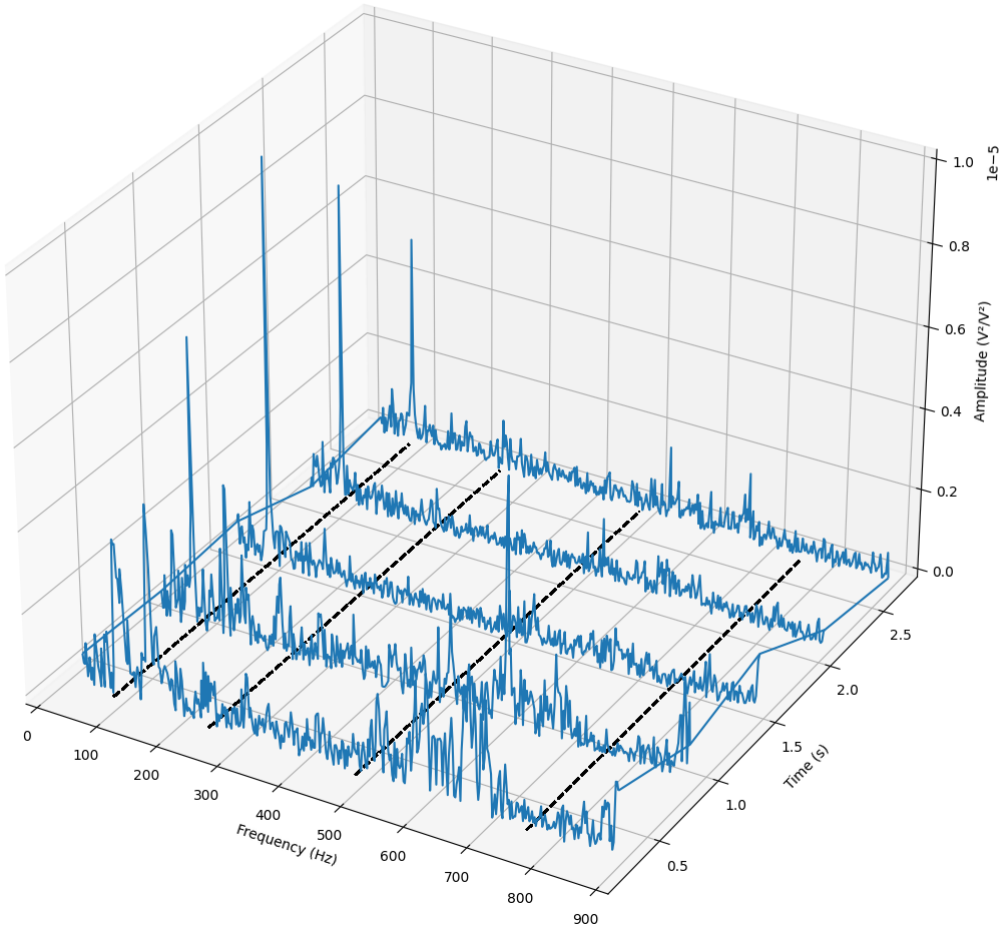

Figure 7. Measured frequency content obtained from specimen 1 (blue lines) compared with theoretical fundamental frequencies (black dashed lines).

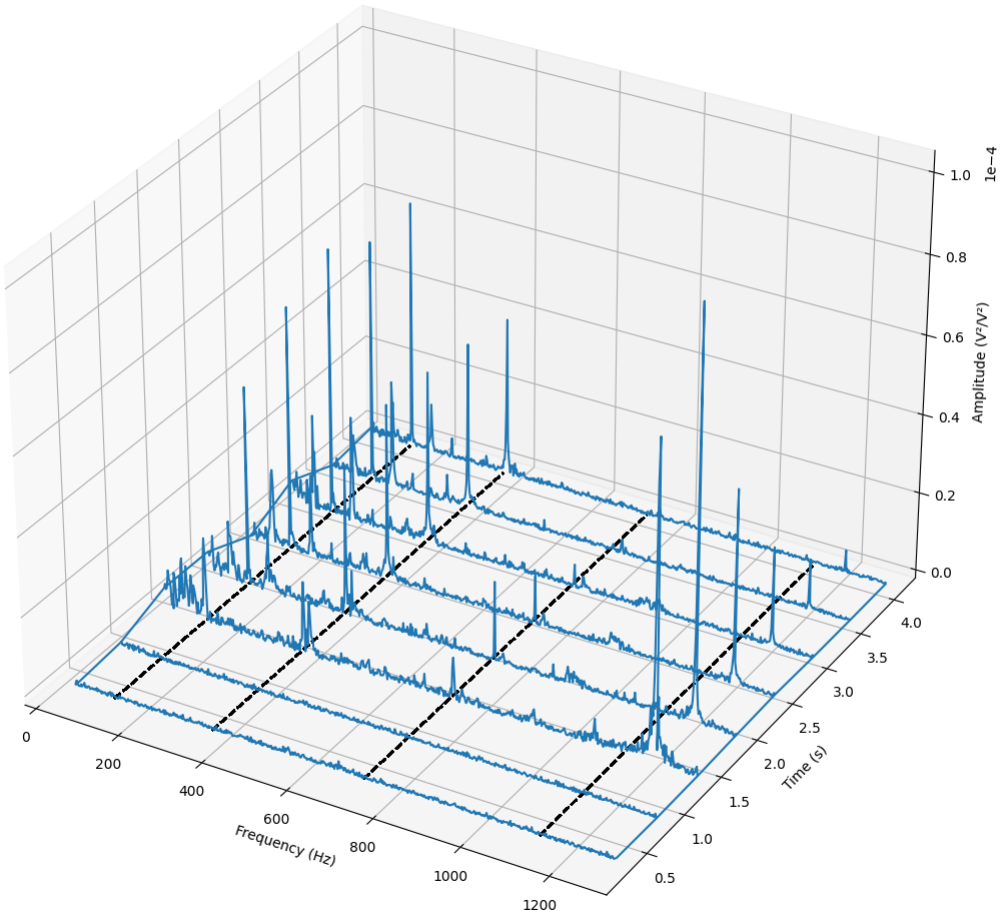

Figure 8. Measured frequency content obtained from specimen 2 (blue lines) compared with theoretical fundamental frequencies (black dashed lines).

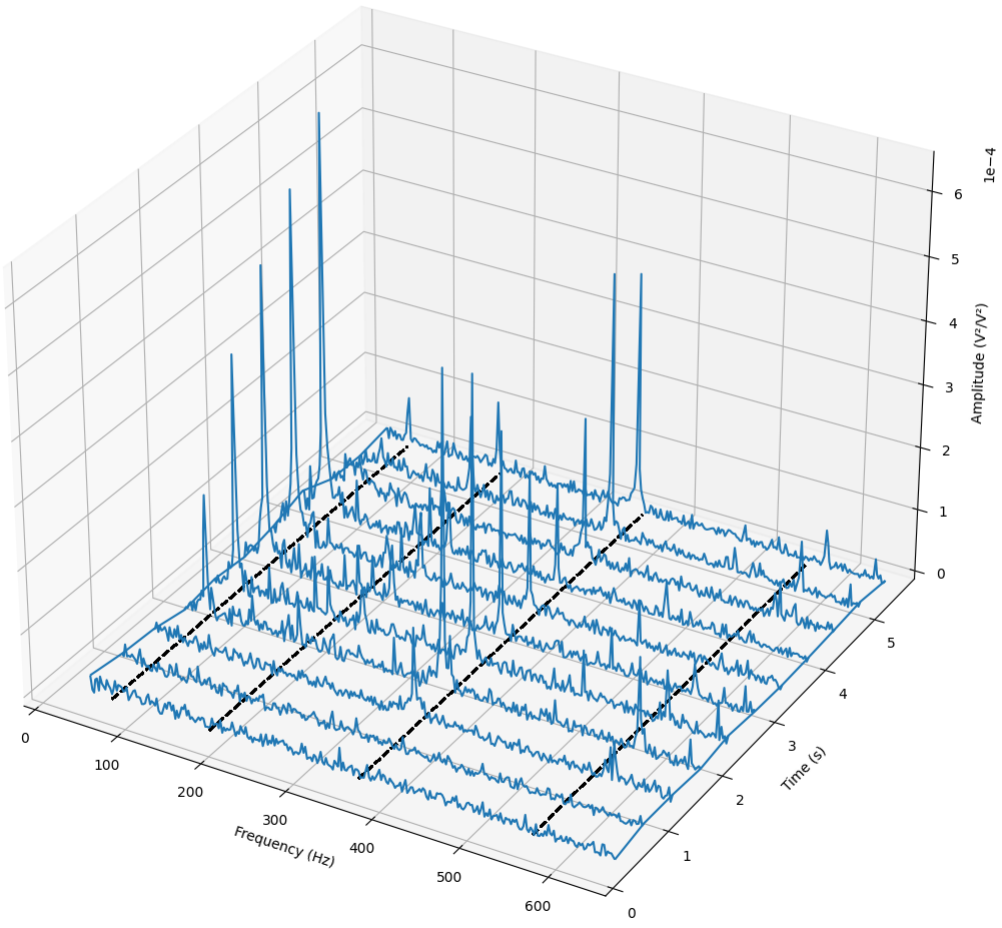

Figure 9. Measured frequency content obtained from specimen 3 (blue lines) compared with theoretical fundamental frequencies (black dashed lines).

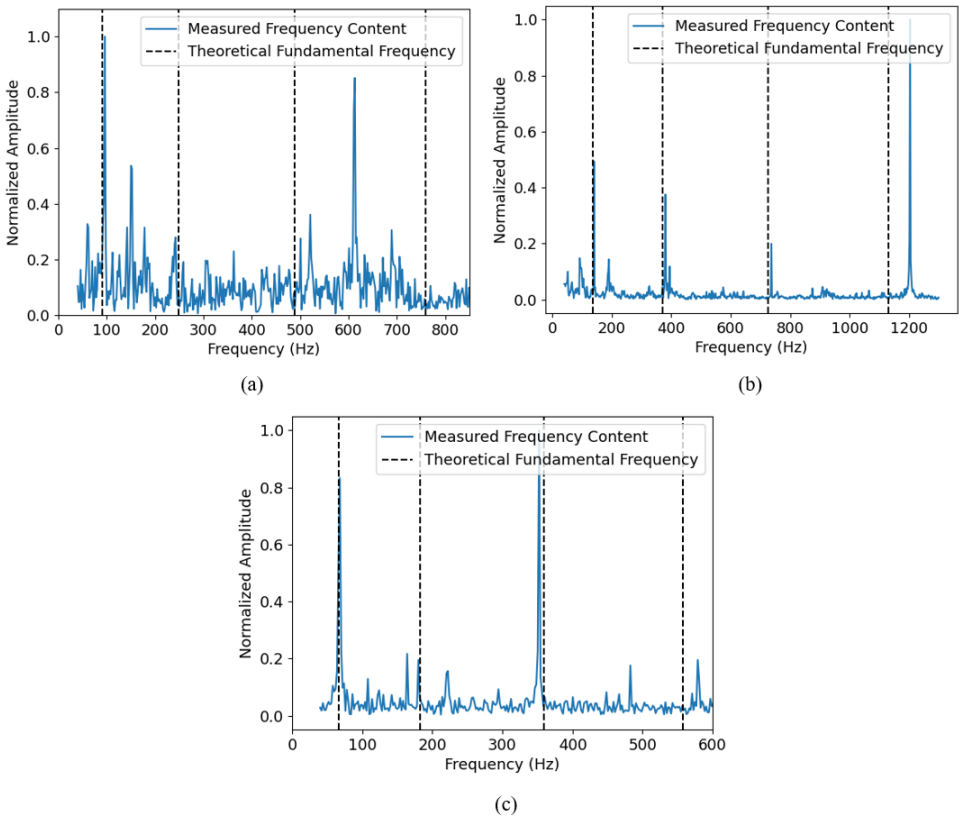

Figure 10. Theoretical fundamental frequencies and measured frequency content over 0.5 s intervals after striking (a) specimen 1, (b) specimen 2, and (c) specimen 3.

third theoretical frequencies, but the agreement between measured vs. theoretical frequencies is generally not as strong in specimen 1 as in specimens 2 and 3. These discrepancies could be related to the relatively weak signal observed from the FPC, as indicated in the optical spectra in Figure 4). This weak signal likely contributed to the lower signal-to-noise ratio in Figure 10 for specimen 1. Alternatively, the bonding between the sensor and the specimen may have affected mechanical strain coupling from the specimen to the sensor. Finally, it is important to note that general discrepancies between theoretical fundamental frequencies and measured peaks could be due to the specimens not perfectly representing a free-free EulerBernoulli beam. All sensors and specimens will be tested to ensure good agreement between measured and theoretical resonant frequencies before introducing structural defects, changing structural boundary conditions, or testing at high temperatures.

5 CONCLUSION

This report summarizes potential sensors, interrogation systems, and bonding techniques for making acoustic measurements of microreactor components for structural health-monitoring purposes. After evaluating the different types of acoustic sensors and the expected constraints of microreactor applications, optical fiber–based sensors were identified as a suitable candidate for in situ acoustic sensing. Sensors such as type-II FBGs and FPCs are two particular optical fiber–based sensors that may be well suited to survive in the extreme environment of a microreactor, which includes high temperatures, neutron fluence, and significant thermomechanical strain. FPC sensors were selected for initial evaluations because of their expected radiation hardness and their compatibility with high-frequency interrogation systems. Preliminary experimental work was conducted to fabricate three FPCs and bond them to pipe and rod specimens to eventually measure vibrational frequencies during high-temperature testing with and without structural defects or changing boundary conditions. Initial room-temperature tests showed that the peaks in the measured frequency spectra obtained experimentally with an LCI interrogation system show good agreement with theoretical fundamental frequencies for two of the three sensors. Future work will perform similar tests at high temperatures to determine whether the FPCs can operate at temperatures relevant to microreactor applications.

6 REFERENCES

[1] David E Shropshire, Geoffrey Black, and Kathleen Araujo. Global market analysis of microreactors. 7 2021.

[2] Shannon M Bragg-Sitton. Next generation nuclear energy: Advanced reactors and integrated energy systems. 4 2022.

[3] Christopher Matthews, Vincent Laboure, Mark DeHart, Joshua Hansel, David Andrs, Yaqi Wang, Javier Ortensi, and Richard C. Martineau. Coupled multiphysics simulations of heat pipe microreactors using direwolf. *Nuclear Technology*, 207(7):1142–1162, 2021.

[4] Jack Douglas Galloway, Valerie Jean Lawdensky, David Irvin Poston, Holly Renee Trellue, and Mikaela E. Blood. Effects of heat pipe failures in microreactors. 6 2020.

[5] Edward M. Duchnowski, Robert F. Kile, Kenny Bott, Lance L. Snead, Jason R. Trelewicz, and Nicholas R. Brown. Pre-conceptual high temperature gas-cooled microreactor design utilizing two-phase composite moderators. part i: Microreactor design and reactor performance. *Progress in Nuclear Energy*, 149:104257, 2022.

[6] Piyush Sabharwall, Jeremy Lee Hartvigsen, Terry James Morton, Zachary Don Sellers, and Jun Soo Yoo. Sphere assembly and operation demonstration. 12 2020.

[7] Holly Renee Trellue, James O'Brien, Robert Stowers Reid, Donna Guillen, and Piyush Sabharwall. Microreactor agile nonnuclear experimental testbed test plan. 1 2020.

[8] Brendan Kochunas and Xun Huan. Digital twin concepts with uncertainty for nuclear power applications. *Energies*, 14(14), 2021.

[9] Gilbert-Rainer Gillich, Nuno M. M. Maia, Magd Abdel Wahab, Cristian Tufisi, Zoltan-Iosif Korka, Nicoleta Gillich, and Marius Vasile Pop. Damage detection on a beam with multiple cracks: A simplified method based on relative frequency shifts. *Sensors*, 21(15), 2021.

[10] Nguyen Tien Khiem and Hai Thanh Tran. A procedure for multiple crack identification in beam-like structures from natural vibration mode. *Journal of Vibration and Control*, 20(9):1417–1427, 2014.

[11] Scott William Doebling, Charles Reed Farrar, and Michael Bruce Prime. A summary review of vibration-based damage identification methods. *The Shock and Vibration Digest*, 30:91–105, 1998.

[12] Onur Avci, Osama Abdeljaber, Serkan Kiranyaz, Mohammed Hussein, Moncef Gabbouj, and Daniel J. Inman. A review of vibration-based damage detection in civil structures: From traditional methods to machine learning and deep learning applications. *Mechanical Systems and Signal Processing*, 147:107077, 2021.

[13] T. Fei, K. Mo, Y. Miao, C. Forsyth, R. Hu, S. Bhattacharya, and T. Kim. Conceptual core design of the molten metal fueled microreactor with self-regulating capability. *Annals of Nuclear Energy*, 173:109112, 2022.

[14] James William Sterbentz, James Elmer Werner, Michael George McKellar, Andrew John Hummel, John Charles Kennedy, Richard Neil Wright, and John Michael Biersdorf. Special purpose nuclear reactor (5 mw) for reliable power at remote sites assessment report. 4 2017.

[15] James W. Sterbentz, James E. Werner, Andrew J. Hummel, John C. Kennedy, Robert C. O'Brien, Axel M. Dion, Richard N. Wright, and Krishnan P. Ananth. Preliminary assessment of two alternative core design concepts for the special purpose reactor. 11 2017.

[16] Christian M. Petrie and Nora Dianne Bull Ezell. Demonstrate embedding of sensors in a relevant microreactor component. 11 2020.

[17] Christian M Petrie, Niyanth Sridharan, Mohan Subramanian, Adam Hehr, Mark Norfolk, and John Sheridan. Embedded metallized optical fibers for high temperature applications. *Smart Materials and Structures*, 28(5):055012, apr 2019.

[18] Dirk Havermann, Jinesh Mathew, William N. MacPherson, Robert R. J. Maier, and Duncan P. Hand. Temperature and strain measurements with fiber bragg gratings embedded in stainless steel 316. *Journal of Lightwave Technology*, 33(12):2474–2479, 2015.

[19] Christian M Petrie, Niyanth Sridharan, Adam Hehr, Mark Norfolk, and John Sheridan. High-temperature strain monitoring of stainless steel using fiber optics embedded in ultrasonically consolidated nickel layers. *Smart Materials and Structures*, 28(8):085041, jul 2019.

[20] E. Luz, C. Gurr-Beyer, and W Stoecklin. Identification of natural frequencies and modes of a nuclear power plant by means of excitation with environment noise. Technical report, Institut für Mechanik (Bauwesen), Universität Stuggart, 1983.

[21] V. Verma, D. Chionis, A. Dokhane, and H. Ferroukhi. Studies of reactor noise response to vibrations of reactor internals and thermal-hydraulic fluctuations in pwrs. *Annals of Nuclear Energy*, 157:108212, 2021.

[22] Mikko Merikoski. Pipe vibrations in nuclear applications. Technical report, Energiforsk, 2017.

[23] Vivek Agarwal, Kyle D. Neal, Sankaran Mahadevan, and Douglas Adams. Concrete structural health monitoring in nuclear power plants. 3 2017.

[24] James A. Smith and Vivek Agarwal. Acoustic measurement infrastructure to characterize nuclear reactor operation. *AIP Conference Proceedings*, 2102(1):060001, 2019.

[25] *On-line Monitoring for Improving Performance of Nuclear Power Plants Part 2: Process and Component Condition Monitoring and Diagnostics*. Number NP-T-1.2 in Nuclear Energy Series. INTERNATIONAL ATOMIC ENERGY AGENCY, Vienna, 2008.

[26] Michel J. Pettigrew. The behaviour of weldable strain gauges under nuclear reactor core conditions. *Nuclear Engineering and Design*, 263:350–361, 2013.

[27] Nina Noppe and Marc Decréton. Strain gauges in a nuclear environment. *Materials & Design*, 14(6):339–341, 1993.

[28] A.N. Sinclair and A.M. Chertov. Radiation endurance of piezoelectric ultrasonic transducers a review. *Ultrasonics*, 57:1–10, 2015.

[29] B. Reinhardt, J. Daw, and B. R. Tittmann. Irradiation testing of piezoelectric (aluminum nitride, zinc oxide, and bismuth titanate) and magnetostrictive sensors (remendur and galfenol). *IEEE Transactions on Nuclear Science*, 65(1):533–538, 2018.

[30] High-dose temperature-dependent neutron irradiation effects on the optical transmission and dimensional stability of amorphous fused silica. *Journal of Non-Crystalline Solids*, 525:119668, 2019.

[31] Christian Petrie, Shay Chapel, Padhraic L. Mulligan, David Bryant, Dan Sweeney, Adam James, N Dianne Bull Ezell, Kurt Smith, Kara Godsey, Maureen Searles, Shawn Stafford, Jeff Arndt, and Jorge Carvajal. Wire-21 sensor irradiation experiment ready for hfir insertion. (ORNL/TM-2022/2354), 2 2022.

[32] Alfredo Güemes, Antonio Fernández-López, and Brian Soller. Optical fiber distributed sensing - physical principles and applications. *Structural Health Monitoring*, 9(3):233–245, 2010.

[33] Yonas Muanenda. Recent advances in distributed acoustic sensing based on phase-sensitive optical time domain reflectometry. *Journal of Sensors*, 2018, 2018.

[34] Kelly McCary, Brandon A. Wilson, Anthony Birri, Thomas E. Blue, and Christian M. Petrie. Suitability of type-ii fiber bragg gratings in silica optical fiber for temperature sensing in treat. 6 2019.

[35] Mohamed A.S. Zaghloul, Mohan Wang, Sheng Huang, Cyril Hnatovsky, Dan Grobnic, Stephen Mihailov, Ming-Jun Li, David Carpenter, Lin-Wen Hu, Joshua Daw, Guillaume Laffont, Simon Nehr, and Kevin P. Chen. Radiation resistant fiber bragg grating in random air-line fibers for sensing applications in nuclear reactor cores. *Opt. Express*, 26(9):11775–11786, Apr 2018.

[36] Jiajun Tian, Yuzhu Jiao, Shaobo Ji, Xiaolong Dong, and Yong Yao. Cascaded-cavity fabryperot interferometer for simultaneous measurement of temperature and strain with cross-sensitivity compensation. *Optics Communications*, 412:121–126, 2018.

[37] Yun Liu, Drew E. Winder, Bing Qi, Cary D. Long, and Wei Lu. Upgraded fiber-optic sensor system for dynamic strain measurement in spallation neutron source. *IEEE Sensors Journal*, 21(23):26772–26784, 2021.

[38] Jinesh Mathew, Oliver Schneller, Dimitrios Polyzos, Dirk Havermann, Richard M. Carter, William N. MacPherson, Duncan P. Hand, and Robert R. J. Maier. In-fiber fabry–perot cavity sensor for high-temperature applications. *J. Lightwave Technol.*, 33(12):2419–2425, Jun 2015.

[39] João Silva, Lucas Nascimento, and Simone dos Santos. Free vibration analysis of euler-bernoulli beams under non-classical boundary conditions. In *IX Congresso Nacional de Engenharia Mecânica*, Fortaleza, Brazil, 2015.

[40] Albrecht Bartels, Arne Thoma, Christof Janke, Thomas Dekorsy, Andre Dreyhaupt, Stephan Winnerl, and Manfred Helm. High-resolution thz spectrometer with khz scan rates. *Optics Express*, 14(1):430–437, 2006.

[41] Daniele Tosi. Review and analysis of peak tracking techniques for fiber bragg grating sensors. *Sensors*, 17(10):2368, 2017.

[42] Daniel C. Sweeney, Anthony Birri, and Christian M. Petrie. Hybrid method for monitoring large Fabry-Pérot cavity displacements with nanometer precision. *Optics Express*, 30(16):29148–29160, Aug 2022.

[43] Ying Huang, Tao Wei, Zhi Zhou, Yinan Zhang, Genda Chen, and Hai Xiao. An extrinsic fabry–perot interferometer-based large strain sensor with high resolution. *Measurement Science and Technology*, 21(10):105308, 2010.

[44] Bing Qi, Drew E Winder, and Yun Liu. Quadrature phase-shifted optical demodulator for low-coherence fiber-optic fabry-perot interferometric sensors. *Optics Express*, 27(5):7319–7329, 2019.

[45] Daniel C Sweeney, Adrian M Schrell, Yun Liu, and Christian M Petrie. Metal-embedded fiber optic sensor packaging and signal demodulation scheme towards high-frequency dynamic measurements in harsh environments. *Sensors and Actuators A: Physical*, 312:112075, 2020.